Journal of Power Sources 246 (2014) 862–867

Contents lists available at ScienceDirect

Journal of Power Sources

journal homepage: www.elsevier.com/locate/jpowsour

In situ synthesis of SnO_2–Fe_2O_3@polyaniline and their conversion to SnO_2–Fe_2O_3@C composite as fully reversible anode material for lithium-ion batteries

Jinxue Guo, Lei Chen, Guangjin Wang, Xiao Zhang*, Fenfen Li

State Key Laboratory Base of Eco-chemical Engineering, College of Chemistry and Molecular Engineering, Qingdao University of Science and Technology, Qingdao 266042, PR China

HIGHLIGHTS

- SnO_2–Fe_2O_3@C nanocomposite is synthesized by a two-step approach.
- In situ polymerization of PANI prevents particle growth in the synthesis.
- Carbonization of PANI guarantees full carbon coating of SnO_2–Fe_2O_3.
- SnO_2–Fe_2O_3@C achieves fully reversible reaction and alloy reaction of SnO_2.
- SnO_2–Fe_2O_3@C shows superior electrochemical properties.

ARTICLE INFO

Article history:
Received 14 June 2013
Received in revised form
30 July 2013
Accepted 14 August 2013
Available online 27 August 2013

Keywords:
Lithium-ion batteries
Anode
Tin oxide
Iron oxide
In situ polymerization

ABSTRACT

We report a two-step approach to synthesize SnO_2–Fe_2O_3@C nanocomposite as a good candidate for high-performance lithium-ion batteries (LIBs) anodes. In this route, the SnO_2–Fe_2O_3@polyaniline is first prepared with in situ polymerization in sol, followed by a carbonized transformation process. The growth of metal oxides particles is firstly suppressed by the polyaniline (PANI) on their outer surface in the in-situ polymerization route and secondly restricted by fully coating of carbon shell in thermal treatment, which forms by in situ carbonization of the polymer. Due to the unique structure and a so-called synergistic effect between SnO_2 and Fe_2O_3, an excellent capacity over 1000 mAh g^{-1} is maintained after 380 cycles at current density of 400 mA g^{-1}. The key insight is that the composite anode presented here achieves fully reversible Li insertion/extraction reaction and maintains high capacity for a long cycling life at high current density, and is realized as promising high-performance LIBs anode materials.

1. Introduction

Rechargeable lithium-ion batteries (LIBs) have been the most widely used power source for portable electronic devices and viewed as the promising source supply of electrical/hybrid vehicles, due to their high energy density, fast charge/discharge rate, and durable cycling stability [1]. Recently, to meet the increasing demands for high-performance LIBs, electrochemically active transition metal oxides such as SnO_2, Fe_3O_4, Fe_2O_3, TiO_2, CuO, and Co_3O_4 have been exploited as promising anode materials for their high theoretical capacity and natural abundance [2–9]. For instance, SnO_2 offers attractive features as LIBs anode for its high theoretical capacity (790 mAh g^{-1}), abundance, low cost, chemical stability, and environmental friendliness. However, the commercialization of SnO_2 electrode is hampered by two major issues: (1) the huge volume changes associated with Li insertion/extraction process result in electrode pulverization problem, causing the quick capacity fading, (2) its poor ionic and electronic conductivities lead to slow charge/discharge rates [10–14]. Over the past few years, many efforts have been made to mitigate these obstacles, such as the controlled synthesis of nanosized SnO_2 with specific size, shape and structure [10,15,16]. The other technique is to design composites of SnO_2 and carbon materials, including graphene, carbon nanotubes, and conductive carbon deriving from thermal decomposition of carbon-containing precursors [7,17–20]. It is suggested that carbon coating not only increases the electronic conduction of the electrode material but also serves as a buffer to prevent the structure collapse induced by the large volume change.

* Corresponding author. Tel.: +86 532 8402 2681; fax: +86 532 8402 3927.
E-mail address: zhx1213@126.com (X. Zhang).

0378-7753/$ – see front matter © 2013 Elsevier B.V. All rights reserved.
http://dx.doi.org/10.1016/j.jpowsour.2013.08.052

Recently, a so-called synergistic effect has been proposed to increase the capacity and stability of SnO_2 [21]. The remaining free spaces between neighboring hybrid nanostructures, which are composed of active/synergetic materials, will increase the capability of electrolyte maintaining and serve as structure stabilizers, thus leading to substantial improvement of Li storage. Thus, a number of metal oxides such as RuO_2, In_2O_3, NiO, Fe_2O_3, and Fe_3O_4 have been employed to prepare SnO_2-based composites to improve the electrochemical performance [22–25].

Inspired by recent works, for the first time, we report the in situ polymerization sol–gel route combined with thermal decomposition conversion process for the synthesis of SnO_2–Fe_2O_3@C. Here, Fe_2O_3 is chosen as the synergetic anode materials due to its abundance, relatively good electronic conduction, high theoretical specific capacity, and environmental benignity [26–28]. Furthermore, the SnO_2–Fe_2O_3 hybrid nanostructures are well coated with conductive carbon shell. All the efforts mentioned above insure that the as-synthesized SnO_2–Fe_2O_3@C nanocomposite displays significantly enhanced kinetics and improved cycling stability as LIBs anode.

2. Experimental

2.1. Sample preparation

All regents are of analytical grade and used as purchased without further purification. The SnO_2–Fe_2O_3@C nanocomposites are prepared via a simple pre-coating process in which the SnO_2–Fe_2O_3 sol is first coated with a conductive polyaniline (PANI) layer by in situ polymerization of aniline, followed by heating at high temperature in air, as shown in Scheme 1. Briefly, 0.01 mol $FeCl_3 \cdot 6H_2O$, 0.03 mol $SnCl_4 \cdot 5H_2O$ and 0.04 mol citric acid are dissolved in 100 ml deionized water. The mixed solution reacts for 6 h at 75 °C. After the resultant yellow sol is cooled to 3 °C, 2.0 ml aniline is added into the sol in 15 min under magnetic stirring. After 3 h, the resultant green gel is aged in air for 12 h at room temperature. Finally, the samples are sintered at 400 °C for 3 h in air to carbonize the PANI precursors and in situ generate metal oxide nanocrystallites. The bare SnO_2–Fe_2O_3 composites are prepared following the same route for comparison.

2.2. Materials characterization

The samples are characterized with X-ray powder diffraction (XRD) by a Philips X′-pert X-ray diffractometer with Cu Kα radiation ($\lambda = 0.154056$ nm). Scanning electron microscope (SEM) is obtained with a JEOL JSM-7500F scanning electron microscope. Transmission electron microscope (TEM) analysis is performed using a JEOL, JEM-2100. Fourier transform infrared (FTIR) spectra are recorded using an FTIR analyzer (Nicolet Magna-IR750). The thermogravimetric analysis (TGA) is measured by a TG2091F from room temperature to 800 °C at a heating rate of 10 °C min^{-1} in air.

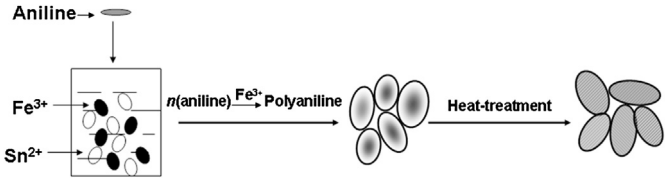

Scheme 1. In situ polymerization of SnO_2–Fe_2O_3@PANI and their conversion to SnO_2–Fe_2O_3@C.

2.3. Electrochemical measurements

The electrochemical tests are carried out with a CR2016-type coin cell. Metallic lithium sheet is used as the negative electrode. The working electrode is fabricated by compressing a mixture of active materials (SnO_2–Fe_2O_3@C and SnO_2–Fe_2O_3), conductive material (acetylene black) and binder polyvinylidene fluoride (PVDF) in a weight ratio of 8:1:1 onto a copper foil at 10 Mpa. The typical mass load of active material is about 1–2 mg cm^{-2}. The electrode is dried at 120 °C for 12 h in vacuum oven and the cell assembly is operated in a glove box filled with pure argon. The Clegard 2300 microporous film is used as separator. The electrolyte solution is 1 M $LiPF_6$ dissolved in a mixture of ethylene carbonate (EC)/dimethyl carbonate (DMC)/ethyl methyl carbonate (EMC) (1:1:1 in volume) (Zhangjiagang, China). Charge–discharge experiments are performed between 3 and 0.01 V on a LAND CT2001A Battery Cycler (Wuhan China).

3. Results and discussion

3.1. Formation of SnO_2–Fe_2O_3@C nanocomposite

The overall synthetic strategy of SnO_2–Fe_2O_3@C is illustrated in Scheme 1. First, SnO_2–Fe_2O_3 sol is prepared through the hydrolysis of corresponding metal salts in a citric acid solution. When aniline is added to the sol, Fe^{3+} ions on the outer surface of SnO_2–Fe_2O_3 colloidal particles lead to the oxidation polymerization of aniline. This process plays a key role in the formation of unique SnO_2–Fe_2O_3@C structure, which effectively enhances its electrochemical performance. In this step, the SnO_2–Fe_2O_3 colloidal particles are completely coated with PANI and their aggregation is restricted by the outer PANI shell, resulting in nanosized particles. So PANI here serves as carbon-containing precursor and restriction of the particle growth. Finally, thermal treatment of the obtained products at 400 °C in air leads to the carbon-coated SnO_2–Fe_2O_3 nanocomposite. During this process, the carbon shell carbonized from the polymer shell restricts the in situ crystallite growth of SnO_2–Fe_2O_3, which occurs frequently in thermal treatment at high temperature. By this means, the nanoparticles are evenly coated with conductive carbon shell. The introduction of carbon layer can enhance the electronic conductivity of the nanocomposite and facilitate enhanced Li^+ transport kinetics. In addition, carbon layer may act as the buffer for the huge volume changes in Li insertion/extraction process.

3.2. Characterization of materials

The powder XRD patterns are obtained to confirm the composition of the as-prepared SnO_2–Fe_2O_3@C composite and are shown in Fig. 1a. The peak located at $2\theta = 18°$can be attributed to the characteristic periodicity perpendicular to the polymer chain of PANI [29], suggesting the residual PANI after the calcination. The other intensive peaks can be well indexed to tetragonal SnO_2 (JCPDS card no. 41-1445) and rhombohedral Fe_2O_3 (JCPDS card no. 33-0664), respectively. The results indicate that SnO_2–Fe_2O_3@C composite could be constructed through this in-situ polymerization route followed by heat treatment process.

The FTIR spectra of SnO_2–Fe_2O_3@PANI (curve A) and SnO_2–Fe_2O_3@C (curve B) are shown in Fig. 1b. In curve A, the peaks at 617 and 471 cm^{-1} corresponding to the M–O–M (M = Fe, Sn) vibrations are observed at low wavenumber region [11,30,31]. In curve A, the characteristic peaks at 1624 cm^{-1} and 1405 cm^{-1} correspond to C=N stretching, the characteristic peak at 1497 cm^{-1} corresponds to a benzenoid C=C, the peak at 1301 cm^{-1} attributes to the stretching vibration of C–N, and the characteristic peak at around

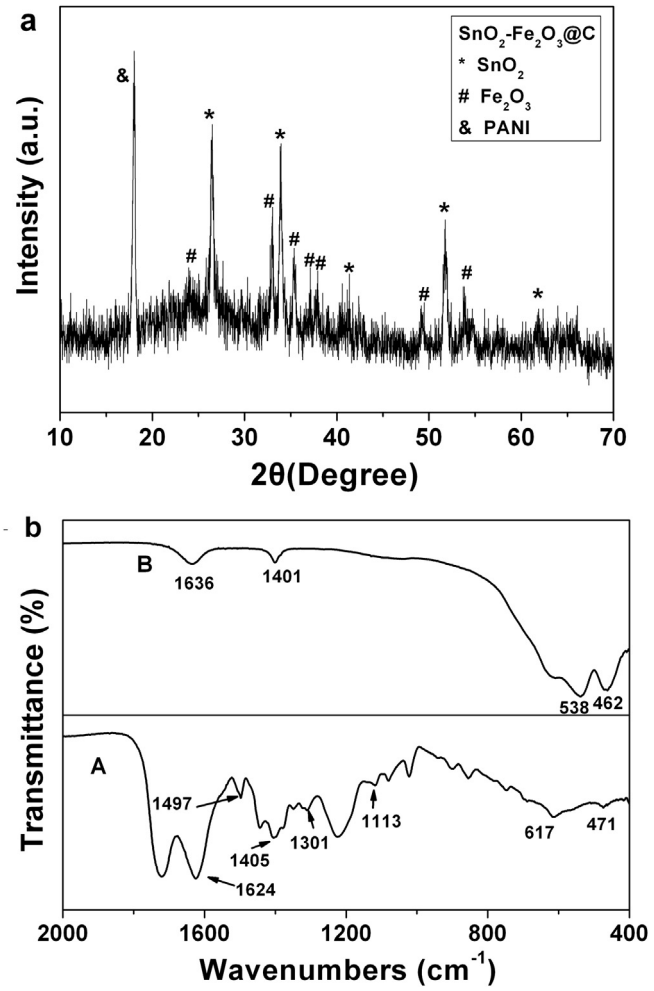

Fig. 1. (a) XRD patterns of as-prepared SnO_2–Fe_2O_3@C composite. (b) FTIR spectra of (A) SnO_2–Fe_2O_3@PANI and (B) SnO_2–Fe_2O_3@C composite.

1113 cm^{-1} assigns to N = Q = N stretching of polyamine [32,33]. This result ascertains the presence of PANI in the as-prepared SnO_2–Fe_2O_3@PANI composite. Curve B displays the prominent peaks at 538 and 462 cm^{-1}, which assigns to Fe_2O_3–SnO_2. More interestingly, the characteristic peaks at 1636 cm^{-1} and 1401 cm^{-1} corresponding to C=N stretching are also observed, indicating that there is residual N in the SnO_2–Fe_2O_3@C composite.

The SEM image in Fig. 2a demonstrates the agglomerate structure of SnO_2–Fe_2O_3@PANI composite, in which a large number of metal oxides particles are connected together with PANI. Fig. 2b shows a selected SEM image of SnO_2–Fe_2O_3@PANI agglomerate, demonstrating that the particles are coated and connected with polymer. Fig. 2c shows the SEM image of SnO_2–Fe_2O_3@C composite, which demonstrates its agglomerate structure. There is no obvious difference between the typical particle sizes of SnO_2–Fe_2O_3@C and SnO_2–Fe_2O_3@PANI composite, indicating the restriction effect of the carbon layer on the particle growth. As shown in the TEM image of SnO_2–Fe_2O_3@C composites (Fig. 2d), the particles are coated with carbon and the carbon layer is distributed in the interstitial particle/boundary region to prevent the agglomeration of particles. The selected TEM image in Fig. 2e shows more clearly that all the metal oxide crystallites are coated with carbon layer (labeled by white arrows), indicating a metal oxides/carbon core–shell structure of SnO_2–Fe_2O_3@C composites. And the metal oxide particles are connected together with the carbon shell (labeled by black arrows), ensuring electrical continuity around the particles. Such specific SnO_2–Fe_2O_3@C structures composed of nanosized particles coated with conductive carbon shell will facilitate the electrolyte diffusion, shorten the path length of electronic and lithium transport, increase the electronic conductivity around the composite, and buffer the volume expansion during Li^+ insertion/extraction process, resulting in enhanced electrochemical properties. The carbon content of SnO_2–Fe_2O_3@C composite is measured with TGA. As shown in Fig. 2f, the TGA curve shows weight loss of 10.7% from 250 to 700 °C, which should be attributed to the oxidation of carbon derived from carbonization of PANI and residual PANI.

3.3. Electrochemical properties

The as-synthesized SnO_2–Fe_2O_3@C nanocomposite and bare SnO_2–Fe_2O_3 nanoparticles are employed as anode materials to assemble laboratory lithium-ion cells. Fig. 3a shows the typical galvanostatic charge and discharge profiles in their 1st cycle at current density of 200 mA g^{-1}. The SnO_2–Fe_2O_3@C nanocomposite anode delivers higher initial discharge capacity and charge capacity of 2506 and 1606 mAh g^{-1} than that of 1175 and 621 mAh g^{-1} for SnO_2–Fe_2O_3 nanoparticles. The composite also shows better initial Coulombic efficiency of 64% than that of 53% for SnO_2–Fe_2O_3, which should be attributed to the carbon coating. There are large capacity losses between the discharge and charge for both anodes in their first cycle, which should be assigned to the formation of Li_2O and solid–electrolyte interface (SEI) layer during the first discharge cycle [34].

As mentioned in ref. 11, the bare SnO_2 suffers from drastic capacity fading with a low capacity of 152 mAh g^{-1} remaining after 20 cycles at a current density of 50 mA g^{-1}. In this paper, Fe_2O_3, which is employed as a synergetic anode material, serves as volume spacers between neighboring SnO_2 to facilitate electrolyte penetration, buffer the volume changes, and reduce the aggregation during Li^+ intercalation, leading to improved electrochemical energy storage performance slightly. As shown in Fig. 3b, the SnO_2–Fe_2O_3 delivers a higher charge capacity of 384 mAh g^{-1} after 20 cycles at a higher current density of 200 mA g^{-1} in comparison with results in ref. 11. However, the capacity of SnO_2–Fe_2O_3 nanoparticles gradually decreases and only remains 167 mAh g^{-1} (25.7% retention of their second capacities) after 150 cycles, which should be attributed to the inevitable pulverization of SnO_2–Fe_2O_3 nanoparticles. In contrast with it, SnO_2–Fe_2O_3@C nanocomposite shows amazing enhanced cycling performance. After 150 successive cycles, the discharge capacity of 1462 mAh g^{-1} (89.2% retention of their second capacities) is observed for SnO_2–Fe_2O_3@C, which is better than most of the SnO_2 based composites reported. Moreover, the Coulombic efficiency of SnO_2–Fe_2O_3@C anode increases to 98% after twelve cycles. Especially from the 88th cycle, the SnO_2–Fe_2O_3@C anode keeps the Coulombic efficiency higher than 99%, demonstrating an excellent reversible Li insertion/extraction performance.

There is also an interesting phenomenon shown in Fig. 3b. The reversible capacity of SnO_2–Fe_2O_3@C anode decreases slightly in its initial 70 cycles and reaches 965 mAh g^{-1}, and then increases significantly and exceeds 1400 mAh g^{-1} after 140 cycles. It is similar to the results reported for SnO_2/C composites and Fe_3O_4/C composites [35,36]. The capacity decrease of the SnO_2–Fe_2O_3@C composites in the first 70 cycles should be attributed to the pulverization of original aggregation of SnO_2–Fe_2O_3 composites during the Li insertion/extraction process, which leads to loss of electrical connectivity between neighboring composite particles. During the discharge/charge cycles, particle sizes of the composite become smaller and smaller due to electrochemical milling effect

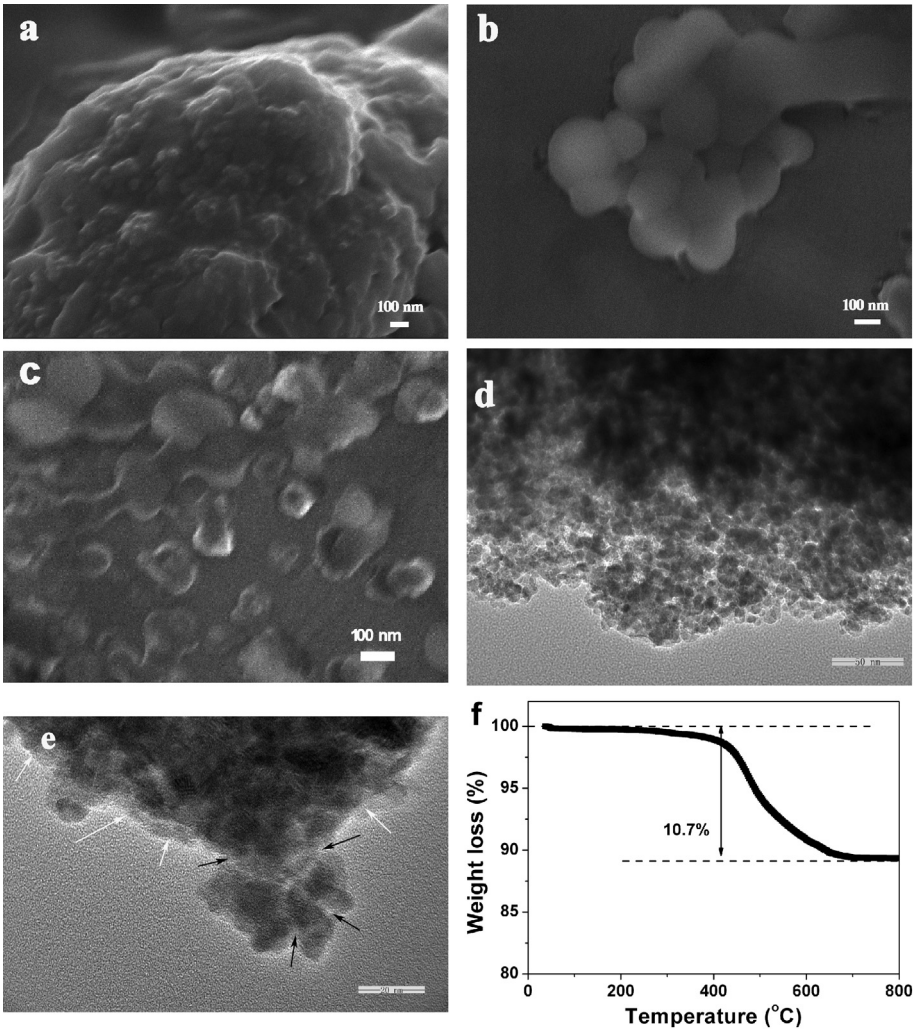

Fig. 2. (a, b) SEM images of SnO_2–Fe_2O_3@PANI. (c) SEM and (d, e) TEM images of SnO_2–Fe_2O_3@C. (f) TGA curve of SnO_2–Fe_2O_3@C composite.

and it attaches to the carbon shell more tightly. It is believed that the decrease of the particle size will facilitate the reversible reaction of the electrode. And the tight contact between the composite particles and the carbon shell can further enhance their electrochemical performance. So the reversible capacity of SnO_2–Fe_2O_3@C composites shows an obvious increase after 70 cycles.

As we all know, the theoretical capacity of Fe_2O_3 (1000 mAh g^{-1}) is calculated based on the following conversion mechanism:

$$Fe_2O_3 + 6Li^+ + 6e^- = 2Fe + 3Li_2O \quad (1)$$

When SnO_2 is used as anode material for LIBs, there are two processes composed of conversion and alloy mechanisms, which could be described as follows:

$$SnO_2 + 4Li^+ + 4e^- = Sn + 2Li_2O \quad (2)$$

$$Sn + xLi^+ + xe^- = Li_xSn (0 \le x \le 4.4) \quad (3)$$

Normally, the theoretical capacity of 790 mAh g^{-1} for SnO_2 is calculated based on the highly reversible alloy reaction of eq. (3). As for conversion reaction of eq. (2), it is usually thought to be electrochemically irreversible and has no contribution to the reversible capacity. Based on the reaction mechanisms mentioned above, the theoretical capacity of SnO_2–Fe_2O_3 is calculated to be 820 mAh g^{-1} (estimated on the mole ratio of SnO_2:Fe_2O_3 = 6:1). It is worth noting that the discharge capacity of SnO_2–Fe_2O_3@C anode is much higher than its theoretical capacity. Recently, Zhao and co-workers have proved the fully reversible conversion reaction of eq. (2) [37]. Thus the theoretical capacity of SnO_2 can be extended from 790 mAh g^{-1} to 1490 mAh g^{-1}, and the relevant theoretical capacity of SnO_2–Fe_2O_3 will be extended to 1420 mAh g^{-1}. In our examined data, the capacities are close to the expected theoretical capacity. So it can be predicated that the SnO_2–Fe_2O_3@C composite demonstrates the completely reversible conversion and alloy reaction of SnO_2. And the overall electrochemical reaction of SnO_2 in SnO_2–Fe_2O_3@C should be described as

$$SnO_2 + 8.4Li^+ + 8.4e^- = Li_{4.4}Sn + 2Li_2O \quad (4)$$

The cyclic capacities of SnO_2–Fe_2O_3@C nanocomposite observed at current density of 100 and 400 mA g^{-1} further confirm the reversible conversion reaction of eq (2). As is shown in Fig. 3c, all the discharge capacities of SnO_2–Fe_2O_3@C anode observed at 100 mA g^{-1} are higher than 1300 mAh g^{-1}, which demonstrates the fully reversible conversion and alloy reaction of SnO_2. When the current density is increased to 400 mA g^{-1}, the discharge capacities of initial three cycles are 1412, 1049 and 977 mAh g^{-1}, respectively. Through a similar process, the capacity of SnO_2–Fe_2O_3@C composite firstly declines then rises to 1000 mAh g^{-1} after 346th cycles

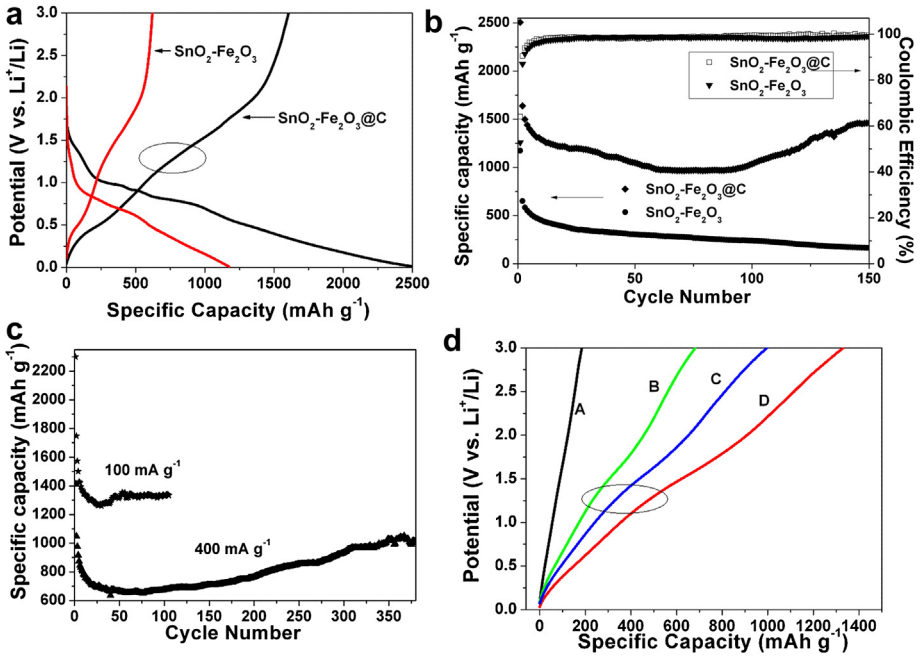

Fig. 3. (a) The first galvanostatic charge–discharge curve and (b) cyclic performances of SnO_2–Fe_2O_3 and SnO_2–Fe_2O_3@C at current density of 200 mA g^{-1}. (c) Cyclic performance of SnO_2–Fe_2O_3@C at current density of 100 mA g^{-1} and 400 mA g^{-1}. (d) The 130th galvanostatic charge curve of SnO_2–Fe_2O_3 at 200 mA g^{-1} (A); the 130th galvanostatic charge curve of SnO_2–Fe_2O_3@C at 400 mA g^{-1} (B); the 346th galvanostatic charge curve of SnO_2–Fe_2O_3@C at 400 mA g^{-1} (C); the 130th galvanostatic charge curve of SnO_2–Fe_2O_3@C at 200 mA g^{-1} (D).

and keeps upon 1000 mAh g^{-1} over 380 cycles, indicating that SnO_2–Fe_2O_3@C delivers partly reversible conversion reaction of eq (2) even at higher current density. To date, such ultra-high reversible capacity with long cycling life is barely observed for the SnO_2 based composite and makes the SnO_2–Fe_2O_3@C composite access to the practical application.

The galvanostatic charge profile provides us a clue to reveal the route of its excellent electrochemical properties. According to the reports [23,27,36–38], de-alloying reaction of eq. (3) only occurs below 1.0 V (vs. Li/Li^+), the conversion reaction of Sn to SnO_2 (eq. (2): $Sn + 2Li_2O = SnO_2 + 4Li^+ + 4e^-$) occurs at around 1.3 V, and the conversion reaction of Fe to Fe_2O_3 occurs at about 1.8 V during the lithium charge process. As shown in Fig. 3a, the charge potential plateau of SnO_2–Fe_2O_3 composite at 1.3 V can be ignored, indicating that the conversion of eq. (2) is not reversible for SnO_2–Fe_2O_3 anode. Bur for SnO_2–Fe_2O_3@C composite, an obvious plateau at around 1.3 V (indexed by ellipse) can be observed, indicating the reversible conversion reaction of eq. (2) for SnO_2–Fe_2O_3@C anode. The galvanostatic charge profiles shown in Fig. 3d further confirm the reversible conversion reaction in eq (2). It can be clearly seen that there is no potential plateau at 1.3 V observed for SnO_2–Fe_2O_3 electrode (curve A). In contrast with it, all the profiles of SnO_2–Fe_2O_3@C anode show a long plateau at around 1.3 V (indexed by ellipse), confirming the reversible conversion of SnO_2–Fe_2O_3@C composite. Taking curve B as an example, although its capacity of 683 mAh g^{-1} is lower than the theoretical capacity of the composite (820 mAh g^{-1}), the 130th charge curve of SnO_2–Fe_2O_3@C anode at current density of 400 mA g^{-1} also delivers the reversible conversion plateau at 1.3 V. In the 346th cycle (curve C), the plateau at 1.3 V is longer than that in curve B, suggesting that the electrochemical performance increases due to reduced particle sizes of the composite and the closer contact between composite and carbon shell with increasing cycle numbers. This result indicates that the specific bimetal oxides-carbon core–shell structure synthesized with the in situ polymerization and carbonization process can facilitate the reversible conversion of Sn to SnO_2, resulting in ultra-high reversible capacity and stable cycleability.

Another surprising enhancement of the SnO_2–Fe_2O_3@C anode is their remarkable rate performance. Fig. 4 presents the rate capabilities of SnO_2–Fe_2O_3@C at variable current rates between 100 and 1600 mA g^{-1}. The discharge capacities of SnO_2–Fe_2O_3@C anode are as high as about 1727, 1290, 1051 and 835 mAh g^{-1} at current density of 100, 200, 400 and 800 mA g^{-1}, respectively. Even at the high specific current of 1600 mA g^{-1}, the SnO_2–Fe_2O_3@C nanocomposite still exhibits high reversible capacities of 611 mAh g^{-1}, which is apparently higher than the theoretical capacity of commercial graphite anode (372 mAh g^{-1}). When the current density returns to the initial 100 mA g^{-1}, the composite anode recovers the specific capacity of more than 1400 mAh g^{-1}, reperforming the completely reversible conversion and alloy reaction of SnO_2. Moreover, there is no noticeable capacity fade even after another 45 cycles, proving good stability of the composite. In comparison with the recently reported SnO_2 based composite [11,19,37–39], the

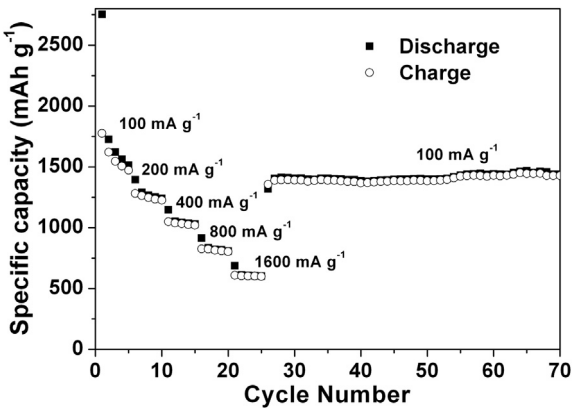

Fig. 4. Rate performance of SnO_2–Fe_2O_3@C at various current densities.

SnO_2–Fe_2O_3@C nanocomposite shows better cyclic performance and rate capability. To the best of our knowledge, the SnO_2–Fe_2O_3@C nanocomposite presented here, which shows outstanding high capacity induced by the fully reversible conversion and alloy reaction of SnO_2, enhanced cycling retention (above 1000 mAh g^{-1} at 400 mA g^{-1} after 380 cycles), and excellent rate performance (611 mAh g^{-1} at 1600 mA g^{-1}), is one of the best SnO_2 based composite ever reported.

4. Conclusions

A facile strategy is presented for the preparation of carbon coated nanosized SnO_2–Fe_2O_3 composite, which seems to be easy to scale up in industrial production. The in situ polymerization of PANI not only prevents the agglomerate and particle growth in sol–gel and thermal treatment processes, but also guarantees the full carbon coating and good conductive contact property between SnO_2–Fe_2O_3 and carbon shell. The unique structure of SnO_2–Fe_2O_3@C nanocomposite effectively improves its electrochemical properties, achieving the fully reversible reaction and alloy reaction of SnO_2. The composites reported herein, which deliver excellent cycling capacity and rate performance, will be a promising candidate as anode materials for LIBs.

Acknowledgments

We gratefully acknowledge the National Natural Science Foundation of China (21003079), Research Award Fund for Outstanding Middle-Aged and Young Scientist of Shandong Province (BS2011CL020), Natural Science Foundation of Shandong Province (ZR2011BM018) and Qingdao Project of Science and Technology (12-1-4-3-(20)-jch) for the financial support.

References

[1] J.M. Tarascon, M. Armand, Nature 414 (2001) 359–367.
[2] P. Poizot, S. Laruelle, S. Grugeon, L. Dupont, J.M. Tarascon, J. Power Sources 97–98 (2001) 235–239.
[3] Z.Y. Guo, X.L. Dong, D.D. Zhou, Y.J. Du, Y.G. Wang, Y.Y. Xia, RSC Adv. 3 (2013) 3352–3358.
[4] X.W. Lou, Y. Wang, C. Yuan, J.Y. Lee, L.A. Archer, Adv. Mater. 18 (2006) 2325–2329.
[5] H.J. Liu, S.H. Bo, W.J. Cui, F. Li, C.X. Wang, Y.Y. Xia, Electrochim. Acta 53 (2008) 6497–6503.
[6] N. Jayaprakash, W.D. Jones, S.S. Moganty, L.A. Archer, J. Power Sources 200 (2012) 53–58.
[7] W.M. Zhang, X.L. Wu, J.S. Hu, Y.G. Guo, L.J. Wan, Adv. Funct. Mater. 18 (2008) 3941–3946.
[8] J.J. Zhang, Y.F. Sun, Y. Yao, T. Huang, A.S. Yu, J. Power Sources 222 (2013) 59–65.
[9] S. Ko, J. Lee, H.S. Yang, S. Park, U. Jeong, Adv. Mater. 24 (2012) 4451–4456.
[10] D. Deng, J.Y. Lee, Chem. Mater. 20 (2008) 1841–1846.
[11] L.F. Cui, J. Shen, F.Y. Cheng, Z.L. Tao, J. Chen, J. Power Sources 196 (2011) 2195–2201.
[12] J.Y. Huang, L. Zhong, C.M. Wang, J.P. Sullivan, W. Xu, L.Q. Zhang, S.X. Mao, N.S. Hudak, X.H. Liu, A. Subramanian, H. Fan, L. Qi, A. Kushima, J. Li, Science 330 (2010) 1515–1520.
[13] J.G. Ren, J.B. Yang, A. Abouimrane, D.P. Wang, K. Amine, J. Power Sources 196 (2011) 8701–8705.
[14] C.M. Wang, W. Xu, J. Liu, J.G. Zhang, L.V. Saraf, B.W. Arey, D. Choi, Z.G. Yang, J. Xiao, S. Thevuthasan, D.R. Baer, Nano Lett 11 (2011) 1874–1880.
[15] C. Wang, Y. Zhou, M.Y. Ge, X.B. Xu, Z.L. Zhang, J.Z. Jiang, J. Am. Chem. Soc. 132 (2010) 46–47.
[16] S.J. Ding, D.Y. Luan, F.Y.C. Boey, J.S. Chen, X.W. Lou, Chem. Commun. 47 (2011) 7155–7157.
[17] L. Cheng, J. Yan, G.N. Zhu, J.Y. Luo, C.X. Wang, Y.Y. Xia, J. Mater. Chem. 20 (2010) 595–602.
[18] Z.M. Cui, L.Y. Jiang, W.G. Song, Y.G. Guo, Chem. Mater. 21 (2009) 1162–1166.
[19] X.J. Zhu, Y.W. Zhu, S. Murali, M.D. Stoller, R.S. Ruoff, J. Power Sources 196 (2011) 6473–6477.
[20] D.W. Kim, I.S. Hwang, S.J. Kwon, H.Y. Kang, K.S. Park, J.J. Choi, K.J. Choi, J.G. Park, Nano Lett. 7 (2007) 3041–3045.
[21] J. Jiang, Y.Y. Li, J.P. Liu, X.T. Huang, C.Z. Yuan, X.W. Lou, Adv. Mater. 24 (2012) 5166–5180.
[22] W.J. Lee, M.H. Park, Y. Wang, J.Y. Lee, J. Cho, Chem. Commun. 46 (2010) 622–624.
[23] J.X. Zhu, Z.Y. Lu, M.O. Oo, H.H. Hng, J. Ma, H. Zhang, Q. Yan, J. Mater. Chem. 21 (2011) 12770–12776.
[24] Q.T. Qu, S.B. Yang, X.L. Feng, Adv. Mater. 23 (2011) 5574–5580.
[25] J. Su, M.H. Cao, L. Ren, C.W. Hu, J. Phys. Chem. C 115 (2011) 14469–14477.
[26] L. Zhang, H.B. Wu, S. Madhavi, H.H. Hng, X.W. Lou, J. Am. Chem. Soc. 134 (2012) 17388–17391.
[27] W.J. Yu, P.X. Hou, F. Li, C. Liu, J. Mater. Chem. 22 (2012) 13756–13763.
[28] Z.Y. Cao, B.Q. Wei, J. Power Sources 241 (2013) 330–340.
[29] Z.M. Zhang, M.X. Wan, Y. Wei, Adv. Funct. Mater. 16 (2006) 1100–1104.
[30] Y.S. Wang, A. Muramatsu, T. Sugimoto, Colloids Surf. A 134 (1998) 281–297.
[31] I.V. Chernyshova, M.F. Hochella Jr., A.S. Madden, Phys. Chem. Chem. Phys. 9 (2007) 1736–1750.
[32] Y.G. Wang, H.Q. Li, Y.Y. Xia, Adv. Mater. 18 (2006) 2619–2623.
[33] H. Liu, X.B. Hu, J.Y. Wang, R.I. Boughton, Macromolecules 35 (2002) 9414–9419.
[34] I.A. Courtney, J.R. Dahn, J. Electrochem. Soc. 144 (1997) 2045–2052.
[35] L. Wang, Y. Yu, P.C. Chen, D.W. Zhang, C.H. Chen, J. Power Sources 183 (2008) 717–723.
[36] P.C. Lian, X.F. Zhu, S.Z. Liang, Z. Li, W.S. Yang, H.H. Wang, Electrochim. Acta 56 (2011) 4532–4539.
[37] Y. Zhao, J.X. Li, N. Wang, C.X. Wu, G.F. Dong, L.H. Guan, J. Phys. Chem. C 116 (2012) 18612–18617.
[38] D.J. Ahn, X.C. Xiao, Y.W. Li, A.K. Sachdev, H.W. Park, A.P. Yu, Z.W. Chen, J. Power Sources 212 (2012) 66–72.
[39] W.W. Xia, Y.W. Wang, Y.F. Luo, J.Y. Li, Y.J. Fang, L. Gu, J.J. Peng, J. Sha, J. Power Sources 217 (2012) 351–357.